American Mineralogist, Volume 95, pages 1132–1140, 2010

Uranyl phosphate sheet reconstruction during dehydration of metatorbernite $[Cu(UO_2)_2(PO_4)_2 \cdot 8H_2O]$

Joanne E. Stubbs,[1,*] Jeffrey E. Post,[2] David C. Elbert,[1] Peter J. Heaney,[3] and David R. Veblen[1]

[1]Department of Earth and Planetary Sciences, Johns Hopkins University, Baltimore, Maryland 21218, U.S.A.
[2]Department of Mineral Sciences, Smithsonian Institution, Washington, D.C. 20560, U.S.A.
[3]Department of Geosciences, Pennsylvania State University, University Park, Pennsylvania 16802, U.S.A.

Abstract

The metatorbernite $[Cu(UO_2)_2(PO_4)_2 \cdot 8H_2O]$ structure comprises autunite-type sheets of corner-sharing uranyl square bipyramids and phosphate tetrahedra, with the interlayer region occupied by Cu^{2+} ions and molecular water. Previous studies have shown that heating induces stepwise dehydration and reduction in basal spacing. Structures of the lower hydrates have not been determined previously because suitable single crystals of these phases have yet to be prepared.

We have used synchrotron X-ray diffraction data collected during in situ, continuous heating of powdered metatorbernite to elucidate structures of its lower hydrates. Using Rietveld analysis, we have determined that autunite-type sheets remain intact through the first dehydration event above room temperature (onset 102 °C). We have discovered that the second dehydration event (onset 138 °C) triggers a major reconstruction to uranophane-type sheets, composed of chains of edge-sharing uranyl pentagonal bipyramids linked to one another by sharing edges and vertices with phosphate tetrahedra. This reconstruction enables the structure to overcome steric constraints on the minimum possible basal spacing, while maintaining Cu within the interlayer.

Four distinct phases have been identified with increasing temperature: $Cu(UO_2)_2(PO_4)_2 \cdot 8H_2O$, space group $P4/n$, a = 6.96519(23), c = 17.3102(8) Å; $Cu(UO_2)_2(PO_4)_2 \cdot 6.1H_2O$, space group $P4/n$, a = 6.95510(29), c = 16.6604(9) Å; $Cu(UO_2)_2(PO_4)_2 \cdot 3H_2O$, space group $P2_1$, a = 14.4979(23), b = 7.0159(9), c = 6.6312(10) Å, β = 107.585(14)°; and a lower hydrate with monoclinic or triclinic symmetry, $a \approx 6.7$, $b \approx 7$, $c \approx 11$ Å, β ≈ 100°. As shown here, in situ heating experiments and the Rietveld method provide fundamental insights into the crystal chemistry and structural behaviors of the important meta-autunite mineral group.

Keywords: Uranium, autunite, torbernite, metatorbernite, meta-autunite, Rietveld, synchrotron X-ray powder diffraction

Introduction

Uranium phosphate minerals of the meta-autunite group $[M(UO_2)_2(PO_4)_2 \cdot nH_2O]$, including metatorbernite (M = Cu, n = 8), are significant hosts for uranium in both natural and anthropogenically contaminated environments (Buck et al. 1995, 1996; Sato et al. 1997; Murakami et al. 1997, 2005; Jerden et al. 2003; Jerden and Sinha 2003; Stubbs et al. 2006, 2009; Catalano et al. 2006; Arai et al. 2007; Zachara et al. 2007; Singer et al. 2009). The metatorbernite structure comprises autunite-type sheets of corner-sharing uranyl square bipyramids and phosphate tetrahedra, with the interlayer region occupied by Cu^{2+} ions and molecular water (Ross et al. 1964; Stergiou et al. 1993; Locock and Burns 2003) (Figs. 1a–1b). Like other members of the meta-autunite group, metatorbernite is variably hydrous, with the prefix "meta-" denoting the partially dehydrated variant that is stable at room temperature in air. Further dehydration occurs when the mineral is heated, and this is accompanied by collapse of the basal (i.e., sheet-to-sheet) spacing (Suzuki et al. 1998, 2005). Similar dehydration can also occur in the high-vacuum environments of instruments (e.g., the transmission electron microscope, or TEM) used to study fine-grained uranium phosphates in soils (Suzuki et al. 1998). Even the moderate heating from specimen interaction with X-rays that occurs during a room-temperature X-ray diffraction experiment can result in dehydration in some meta-autunite minerals (Locock et al. 2005).

Previous studies have addressed the dehydration behavior of metatorbernite and other meta-autunite-group minerals using powder X-ray diffraction (XRD) from heated samples, with patterns recorded both at elevated temperature and at room temperature after heating (Beintema 1938; Takano 1961; Butt and Graham 1981; Suzuki et al. 1998, 2005; Sowder et al. 2000). In all of these studies, only changes in basal spacing were measured, and the authors did not determine or refine the full crystal structures. This is because crystals of the lower hydrates that are suitable for single-crystal diffraction have yet to be prepared, and in powder form the samples suffer from severe preferred orientation effects due to their perfect cleavage parallel to the sheets. It has been generally assumed that the structures of the

* Present address: Stanford Synchrotron Radiation Lightsource, Menlo Park, California 94025, U.S.A. E-mail: jstubbs1@jhu.edu

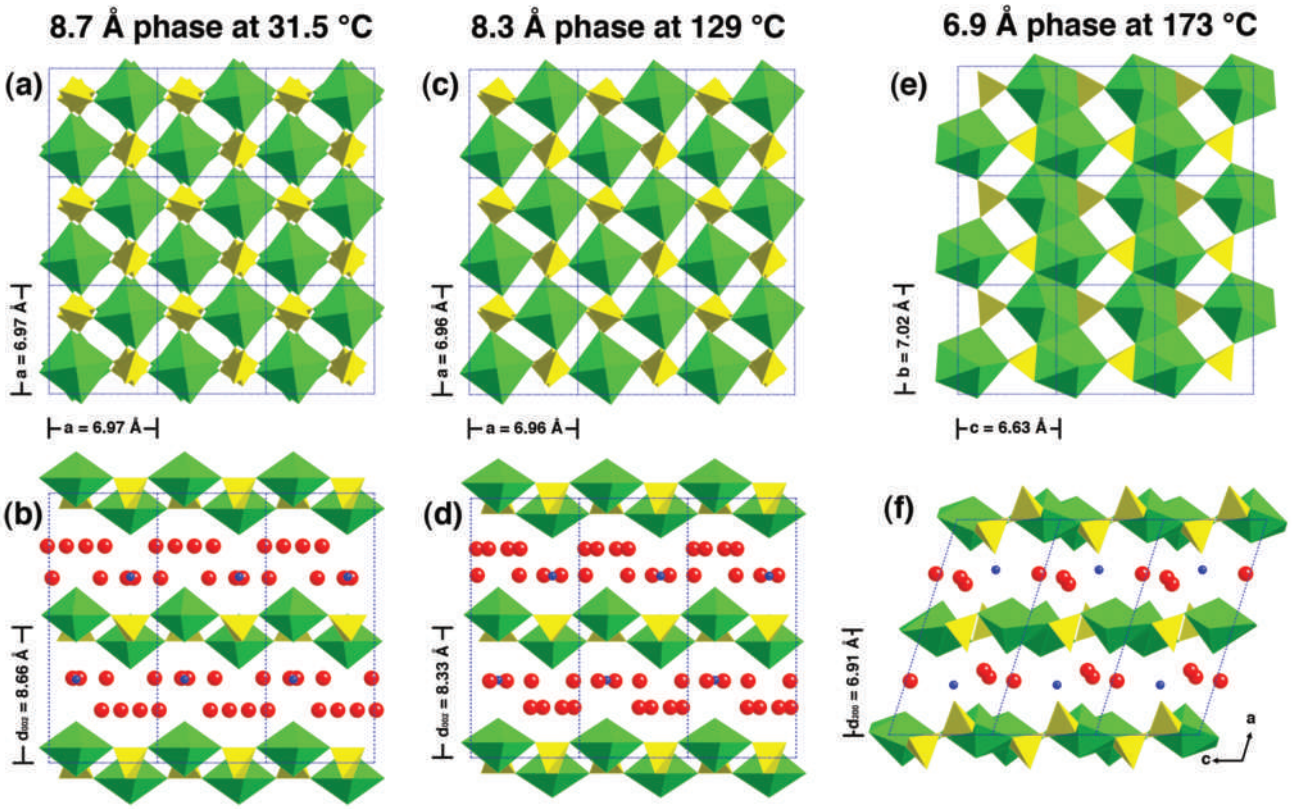

FIGURE 1. Polyhedral representations of the 8.7 Å metatorbernite (**a**–**b**), 8.3 Å (**c**–**d**), and 6.9 Å (**e**–**f**) phases. Green = U, yellow = P, blue = Cu, red = water O. Autunite-type sheets of the 8.7 and 8.3 Å phases (viewed down [001] in **a** and **c**; [010] in **b** and **d**) are similar to one another; minor rotations of the polyhedra distinguish the two. Autunite-type sheets are corrugated in two dimensions (along vector **a**), with morphologies like egg cartons. Uranophane-type sheets of the 6.9 Å phase (single sheet at $x \approx 0.5$ viewed along [100] in **e**, full structure viewed along [010] in **f**) are uncorrugated and can be stacked more closely.

sheets remain intact (Butt and Graham 1981; Suzuki et al. 1998, 2005) and that dehydration entails a simple collapse of the basal spacing, as H_2O is removed.

The dehydration sequence of metatorbernite, as described by Suzuki et al. (1998, 2005), is shown in Table 1, along with basal spacings for metatorbernite and the fully hydrated torbernite (n = 12) from the single-crystal structure determinations of Locock and Burns (2003), and those measured using selected area electron diffraction (SAED) in the TEM at room temperature (Suzuki et al. 1998; Stubbs 2009). If the structure simply collapses along the direction perpendicular to the sheets (**c**), there is insufficient space for the Cu atoms to remain in their sites in the most dehydrated phases. The Cu atoms in metatorbernite are coordinated axially by uranyl-group O atoms from the adjacent sheets, and they are coordinated equatorially by 4 H_2O molecules. Suzuki et al. (1998, 2005) reported basal spacings in the lowest hydrates of 6.8, 6.6, 6.5, and 5.6 Å. A simple collapse of the structure along **c** would require Cu-O_{axial} bond distances ≤1.6 Å in these phases. Most of the Cu-O distances in Cu^{2+}-oxides listed in the Inorganic Crystal Structure Database (ICSD) are ≥1.8 Å. Dehydration of metatorbernite, therefore, very likely involves a change in the interlayer structure, a change in the sheet structure, or both.

In addition, the shortest sheet-to-sheet O-O distances (~2.0 Å) in the lowest hydrate reported by Suzuki et al. (1998, 2005) would be physically unreasonable if the structure simply collapsed along **c**. Because the sheets in room-temperature metatorbernite are already stacked in the manner that permits their closest interplanar spacing, any lateral shifts or rotations would require deformation or reconstruction of the sheets. No study has addressed these steric constraints on the dehydration behavior of metatorbernite or any other meta-autunite-group mineral. Understanding the full range of possible structures under a variety of temperature conditions and H_2O activities is essential to their correct identification. This study also aims to elucidate the structural relationships between the meta-autunite group and other uranyl mineral groups.

TABLE 1. Previously reported basal spacings for torbernite, metatorbernite, and lower hydrates

		Locock and Burns (2003)		Suzuki et al. (1998)		Suzuki et al. (2005)		Stubbs (2009)	
Phase	n	B.S. (Å)	*T* (°C)	B.S. (Å)	*T* (°C)	B.S. (Å)	*T* (°C)	B.S. (Å)	*T* (°C)
Torbernite	12	10.4	RT, wet						
Metatorbernite	8	8.68	RT			8.61	RT	8.64	TEM
Unnamed lower hydrates	4			8.2	55–85	8.07	100		
	2			6.8	65–270	6.58	200	6.71	TEM
↓				6.8	TEM	6.52	300		
	1					5.6	300		
	0			5.7	>280				

Note: n = Number of H_2O per formula unit; B.S. = basal spacing; RT = room temperature; TEM samples likely heated in electron beam.

The present investigation applied in situ heating experiments and synchrotron powder XRD, which do not impart the same experimental challenges that have confronted previous studies. The high X-ray flux available at modern synchrotron sources, such as the National Synchrotron Radiation Light Source (NSLS) at Brookhaven National Laboratory (BNL), allows for the rapid acquisition of powder patterns, and hence the study of evolving mineral structures during continuous heating. Preferred orientation effects were minimized by placing a powdered sample into a glass capillary, which was continuously rotated, and by the use of a 2-D imaging plate for X-ray detection. Proposed structure models for the heated phases were verified and refined by fitting the full powder patterns using the Rietveld method.

EXPERIMENTAL METHODS AND STRUCTURE REFINEMENT

Sample characterization by EMPA

A specimen of natural metatorbernite was provided by the Smithsonian Institution's National Museum of Natural History (no. 127703; Bois Noirs, France). Ratios of the major and minor cations to 12 O atoms (ignoring H_2O) were measured using electron microprobe analysis (EMPA). All Cu was assumed to be divalent, all P and As (which substitutes for P in minor amounts) pentavalent, and all U hexavalent. Flakes of metatorbernite were glued to a glass slide, their basal cleavage surfaces gently cleaned using 3M Post-It adhesive, then carbon coated prior to analysis. The JEOL 8600 Superprobe at Johns Hopkins was operated at 20 kV and 5 nA beam current with a 5 μm beam. Data from 50 points were collected and processed using the program Probe for Windows (PFW; Probe Software, Inc.). EMPA of meta-autunite group minerals is complicated by the loss of H_2O and migration of interlayer cations during analysis (Graham et al. 1984; Stubbs et al. 2007), but corrections for mobile element loss (or gain) can be used to determine initial count rates (e.g., Stormer et al. 1993).

Individual analyses that included 50 consecutively recorded 1 s count intervals were measured, as well as background count rates for 15 s each on either side of the element peaks. The "self-volatile element" correction scheme in PFW was used to fit the natural logarithms of the count rates in the 1 s intervals vs. time with a quadratic function, to determine the count rate extrapolated to zero time. An alternate volatile element correction scheme, in which the exponential decay or increase of count rates is fit with a function that takes into account an eventual steady-state count rate, was also applied to the data and produced identical results to those of PFW. This alternate method provides accurate metatorbernite analyses even when the PFW method fails, as verified by laser ablation inductively coupled mass spectrometry (LA-ICP-MS) (Stubbs et al. 2007).

Powder X-ray diffraction

Synchrotron powder XRD data were collected at the NSLS at beamline X7B. The X-ray wavelength was determined as 0.3184 Å using silicon, corundum, and lanthanum hexaboride NIST standards. The metatorbernite specimen was ground in an agate mortar and pestle under ethanol, allowed to dry, and loaded into a 0.7 mm glass capillary to randomize particle orientations. Preferred orientation effects were further minimized by sample rotation and full intensity integration of the diffraction rings collected using a MAR imaging plate detector. The specimen was continuously heated from 31.5 to 315 °C over the course of 120 min. Temperature was controlled with an Omega 3200 controller attached to a forced air heater and monitored with a chromel-alumel thermocouple adjacent to the sample. Known phase transitions and melting point temperature of $NaNO_3$ between 100 and 310 °C were used for temperature calibration. The calculated calibration curve revealed that the measured temperature was accurate to within an uncertainty of about 3 °C across the study range. Images were integrated into intensity vs. 2θ plots with the program Fit2D (Hammersley et al. 1996) using a polarization factor of 0.93. Diffraction patterns were collected every 3 min, 40 s (i.e., every 9.3 °C), and the collection of each exposure took 60 s.

Structure determination and refinement

Rietveld refinement was carried out using the General Structure Analysis System (GSAS) of Larson and Von Dreele (2004) and the user interface EXPGUI (Toby 2001). The 31.5 °C phase was refined first, using the structure of Locock and Burns (2003) as a starting point. The program Crystal Cracker, build 189 (K. Leinenweber, Arizona State University, http://multianvil.asu.edu/Crystal_Cracker/CrystalCracker.html) was used to determine lattice parameters, and indications of centered cells as ascertained by systematically absent diffraction peaks, for the heated structures. Previous studies have suggested that the autunite-type sheets remain intact when meta-autunite-group minerals are dehydrated (Butt and Graham 1981; Suzuki et al. 1998, 2005), and this was initially presumed to be true. Several structure models were proposed for each of the dehydrated phases, and refinement of these proposed structures was attempted. It is important to note that Rietveld refinement is not a structure determination technique and cannot provide a unique structure solution. However, it is a powerful technique for assessing the plausibility of a proposed structure model and for refining the model.

In the lower hydrates, Le Bail fits (Le Bail et al. 1988) were conducted prior to some Rietveld refinements. This procedure ignores atoms and their positions, instead assigning weights to overlapping reflections according to their multiplicities. It allows for the refinement of unit-cell, background, zero-shift, and peak profile parameters when atom positions are unknown. Following the Le Bail fit, these parameters were fixed while atom positions and scale factor were refined using the Rietveld method. The parameters fit using the Le Bail method were then refined again using the Rietveld method, once the structure had been better determined. This procedure was followed to minimize biasing profile and background parameters by an assumed structural model and as a check of the validity of a particular unit cell.

For each refinement, the background was fit using a shifted Chebyschev function with 8–12 terms. An absorption coefficient, based on the composition of metatorbernite and the diameter of the capillary, was estimated and fixed. Zero-shift and scale factors were refined. Peak shapes were modeled with a pseudo-Voigt profile function as parameterized by Thompson et al. (1987) with asymmetry corrections by Finger et al. (1994) and microstrain anisotropic broadening terms by Stephens (1999). All atom positions (except hydrogen) were refined. Soft bond length and angle restraints were set to maintain U-O_{axial} bond lengths ~1.8 Å (e.s.d. = 0.05), uranyl ion bond angles ~180° (e.s.d. = 2), and U-$O_{equatorial}$ lengths ~2.3–2.4 Å (e.s.d. = 0.1), consistent with published values for uranyl minerals (Burns 2005). Additional soft restraints were used to maintain P-O distances ~1.53 Å (e.s.d. = 0.05) and O-P-O angles in phosphate tetrahedra between 100 and 120° (restraint value = 109°, e.s.d. = 3), consistent with published values for a wide range of phosphates (Baur 1974).

Initial heavy restraint weighting factors (50–100 for distances, 10 for angles) were slowly eased as the refinements progressed, but could not be removed entirely without these bond lengths and angles taking on physically unrealistic values. Because uranium is the overwhelmingly dominant scatterer of X-rays, the precise determination of oxygen positions in metatorbernite is challenging with powder X-ray diffraction and Rietveld refinement methods, and this problem is offset by applying the soft restraints for these bond lengths and angles to well-established values. Initial occupancies for Cu, P, and As were set to the values determined by EMPA and later refined. Initial H_2O occupancies were set to those determined by Suzuki et al. (2005) and subsequently refined. Occupancy factors were not allowed to take on values <0 or >1. In the lower hydrates, Fourier difference maps were used to locate Cu atoms and to aid in proposing positions for H_2O oxygen atoms. Fourier difference maps generated using observed and calculated structure factors derived from Rietveld refinements can provide useful information, but typically less so than for comparable maps from single-crystal studies. This is because the "observed" intensities can be biased by the structure model for severely overlapping Bragg reflections due to the way in which the Rietveld program derives "observed" intensities. Although the refined total H_2O occupancies (i.e., hydration states) and positions are probably approximately correct, the information about the H_2O molecules might be more accurately determined using neutron powder diffraction in a future study.

Isotropic temperature factors were constrained to be equal for cations of a given type, for uranyl-group O atoms, and for O atoms in phosphate tetrahedra. These can correlate strongly with the background parameters, and the strongly scattering U makes refinement of details for O atoms difficult. Thus, in some cases the thermal parameters had to be fixed to physically meaningful values (when they refined to near-zero, negative, or unrealistically large numbers).

Estimated standard deviations, as reported by GSAS, are given in parentheses throughout the text and tables.

RESULTS AND DISCUSSION

Electron microprobe analysis

EMPA results were calculated on an atom basis and normalized to 12 O atoms (ignoring H_2O). The calculated Cu:U:P:As

ratios are 0.98(6):1.96(7):1.9(1):0.11(2). Arsenic is presumed to substitute only for P in the tetrahedral sites. Thus, the calculated Cu:U:P+As ratios are 0.98:1.96:2.05, close to the ideal 1:2:2. Based on the EMPA results, Rietveld refinements were initiated with the occupancy of the Cu site ($Occ._{Cu}$) = 0.98, $Occ._{U}$ = 1, $Occ._{P}$ = 0.95, and $Occ._{As}$ = 0.05. Positions for P and As were constrained to be identical.

Heating study

Diffraction patterns from the heating study are shown in Figures 2 and 3. Four distinct phases were identified with increasing temperature, the most intense diffraction peaks of which correspond to *d*-spacings ~8.7 Å (31.5–120 °C), 8.3 Å (102–164 °C), 6.9 Å (138–315 °C), and 5.4 Å (209–315 °C). These values are comparable to those of Suzuki et al. (2005), who measured basal spacings of 8.61 Å at room temperature (RT), 8.07 Å at 100 °C, 6.58 Å at 200 °C, and 6.52 and 5.60 Å at 300 °C in their heating study of oriented, powdered metatorbernite (Table 1).

As heating proceeded, continuous migration of diffraction peaks was not observed. Instead, discrete transitions between phases occurred, consistent with previous studies (Suzuki et al. 1998, 2005). Peaks broadened, probably because the crystallites fractured into ever-smaller domains during dehydration. There was also a significant loss in overall intensity in the patterns at increased temperatures. This may be attributed to a decrease in long-range positional order of some atoms, increased thermal motion, the loss of H_2O and possibly Cu from the structures, or may simply be due to the formation of different structures, which diffract differently, at higher temperature.

There are considerable overlaps in the temperature ranges over which the phases existed (Fig. 4). These overlaps may be attributed, in part, to the containment of the sample in a glass capillary. Although the end of the capillary was not sealed, rapid evacuation of H_2O was likely hindered, resulting in elevated humidity around the powder particles. Suzuki et al. (2005) also observed the coexistence of multiple phases at some temperatures, despite exposing their samples (mounted on Cu slides) to a continuous flow of N_2 gas. In both studies, the temperature overlaps may be partly due to kinetic effects arising from relatively rapid heating rates. Observed temperature ranges are likely heavily influenced by the experimental setup and should not be interpreted as equilibrium stability fields. The structures of the 8.7, 8.3, and 6.9 Å phases were refined using patterns in

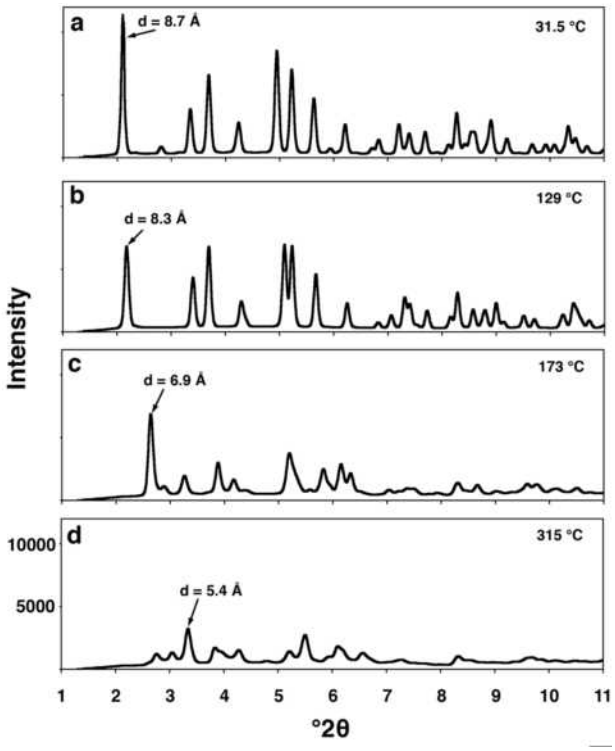

FIGURE 3. Diffraction patterns used for structure refinements plotted from 1–11 °2θ. (**a**) 31.5, (**b**) 129, (**c**) 173, and (**d**) 315 °C. Intensity scale is the same in all 4 patterns.

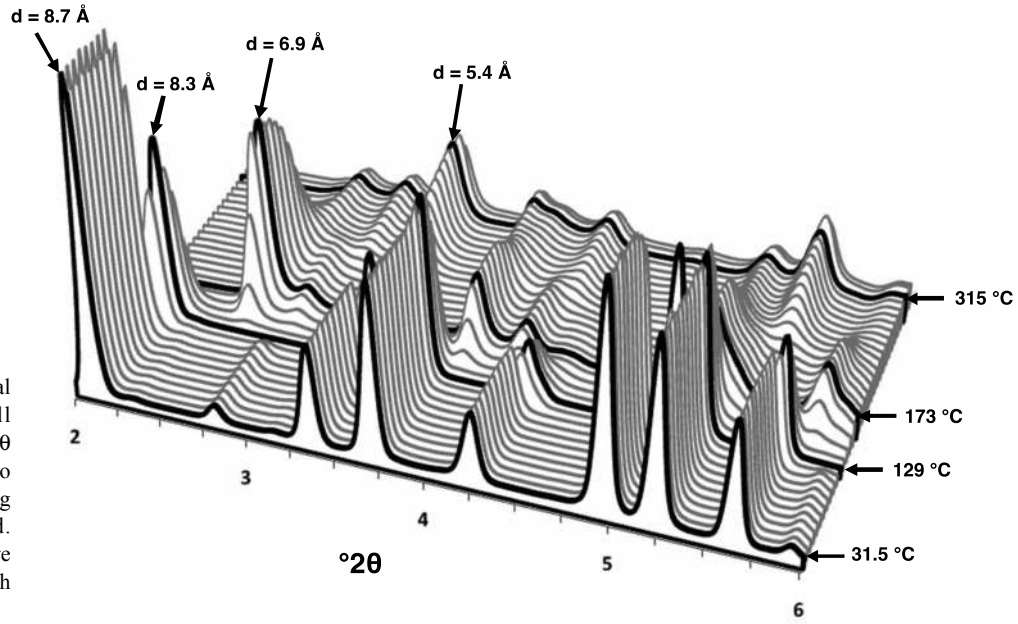

FIGURE 2. Three-dimensional perspective plot showing all diffractograms over 2–6 °2θ with increasing temperature into the page. Peaks corresponding to basal spacings are labeled. The patterns used for structure refinement are highlighted with bold lines.

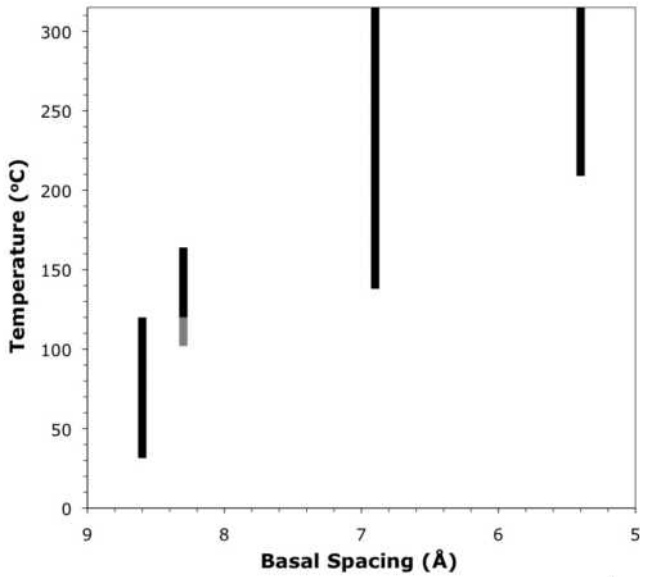

FIGURE 4. Graphical representation of the ranges of temperatures over which the 8.7, 8.3, 6.9, and 5.4 Å phases were observed. Considerable overlaps occurred in which two phases coexisted. The shaded region at the lower end of the line for the 8.3 Å phase indicates temperatures over which the phase's presence was in question.

which the phases occurred singly. The refinement of mixtures yielded unreliable results and was not carried out. The 5.4 Å phase never existed by itself, but at 315 °C the intensity of the 6.9 Å peak (a weak shoulder on the left-most peak visible in Fig. 3d) was quite small.

8.7 Å phase at 31.5 °C. At 31.5 °C, the powder was made up entirely of metatorbernite with an 8.7 Å basal spacing. The structure of this phase (Figs. 1a–1b) was refined using the single-crystal structure of Locock and Burns (2003) as a starting model. The (002) reflection occurred at a small value of 2θ (near the beam stop), and thus could not accurately be fit. It was, therefore, excluded from the refinement. The refined structure is in excellent agreement with that of Locock and Burns, establishing the viability of Rietveld refinement for the study of these structures. The final fit is shown in Figure 5a, refinement parameters in Table 2, and atom positions in Table 3. Occupancies for the Cu, P, and H_2O oxygen atoms all refined to values slightly larger than 1 (likely due to correlation with thermal factors and background parameters), and the U occupancy refined to ~1. All were, therefore, fixed at 1. The occupancy for As refined to a slightly negative number, and was fixed at 0. If As occupancies were fixed at 5%, P occupancies refined to values <90% and As temperature factors refined to values >0.2. Fixing the sum of P and As occupancies to 1, and constraining the P and As temperature factors to be equal also resulted in non-physical refinement parameters. Although EMPA indicated the presence of As (~5% of the tetrahedral cations), the electron beam sensitivity of metatorbernite (Stubbs et al. 2007) introduces additional uncertainty into the analytical results beyond that reported by PFW, and the real As occupancy might be <5%. Occupancies refined by the Rietveld method are also subject to uncertainty, as they can correlate with temperature factors and background parameters. The true As occupancy probably lies between 0 and 5%.

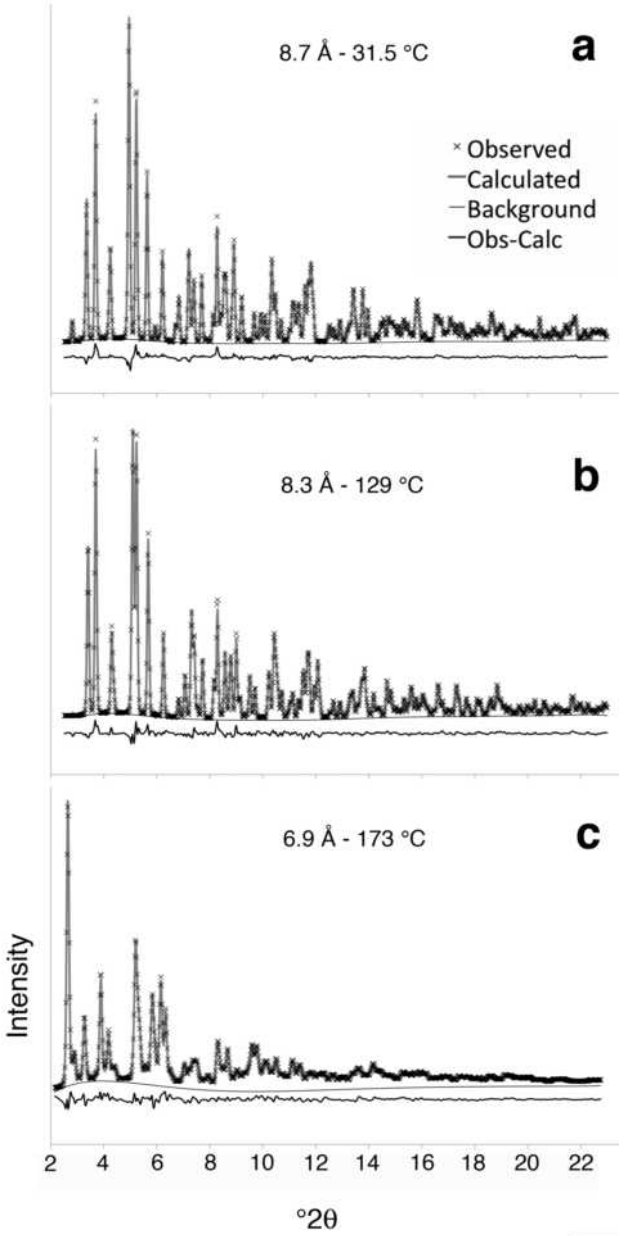

FIGURE 5. Rietveld fits and difference plots for the 8.7, 8.3, and 6.9 Å phases. (002) reflections were excluded from the 8.7 and 8.3 Å refinements (see text for discussion). Minor peak width errors are likely due to metatorbernite's platy habit and resultant anisotropic peak broadening, which is modeled well but imperfectly by GSAS.

Refinement of the 8.7 Å structure model using patterns collected up to 94 °C resulted in structures nearly identical to that of the phase at 31.5 °C, with modest expansion in the *a*- and *c*-dimensions (by 0.0047 and 0.0070 Å, respectively) and no detected loss of interlayer H_2O.

8.3 Å phase at 129 °C. Although the 8.3 Å phase first appeared at 102 °C and was still present at 164 °C, it occurred as a single phase (i.e., not mixed with either the 8.7 or 6.9 Å phase) only at 129 °C. The diffraction pattern collected at this temperature was therefore used for the determination and refinement of the structure. The starting structural model for the 8.3 Å phase was based on the structure of the 8.7 Å phase, assuming that the

TABLE 2. Final Rietveld refinement parameters for the structures at 31.5, 129, and 173 °C

	8.7 Å phase (31.5 °C)	8.3 Å phase (129 °C)	6.9 Å phase (173 °C)
Space group	*P4/n*	*P4/n*	$P2_1$
Unit cell			
a	6.96519(23)	6.95510(29)	14.4979(23)
b			7.0159(9)
c	17.3102(8)	16.6604(9)	6.6312(10)
β			107.585(14)
V (Å^3)	839.78(8)	805.92(9)	642.98(16)
No. of waters pfu	8	6.1	3
Refinement			
No. of data points	1033	1033	1079
No. of reflections	935	902	1532
Diffraction range (*d* Å)	0.799–7.3	0.799–7.3	0.799–8.3
No. of variables	46	48	92
$R(F^2)$	0.0397	0.0504	0.0289
R_{wp}	0.0387	0.0448	0.0481
χ^2	1.29	1.62	2.091
Final bond length restraint weighting factor	5	5	5
Final bond angle restraint weighting factor	n/a due to space group	n/a due to space group	3

TABLE 3. Atomic coordinates and isotropic displacement parameters for the 8.7 Å phase (31.5 °C)

Atom	x	y	z	U_{iso} (Å^2)
Cu1	0.25	0.25	0.3092(5)	0.0072(17)
O1	0.25	0.25	0.4474(13)	0.01*
O2	0.25	0.25	0.9484(13)	0.01*
O3	0.25	0.25	0.6521(12)	0.01*
O4	0.25	0.25	0.1542(12)	0.01*
O5	0.299(5)	0.9083(23)	0.0571(12)	0.01*
O6	0.215(6)	0.9304(22)	0.5482(12)	0.01*
O7 (water)	0.5280(19)	0.2797(32)	0.3147(13)	0.01*
O8 (water)	0.3392(22)	0.5149(21)	0.8048(16)	0.01*
P1	0.25	0.75	0	0.0138(20)
P2	0.25	0.75	0.5	0.0138(20)
U1	0.25	0.25	0.05242(19)	0.00830(35)
U2	0.25	0.25	0.55092(20)	0.00830(35)

* U_{iso} for all O atoms refined to negative or near zero values, so they were fixed at 0.01 Å^2.

decrease in basal spacing resulted from a simple collapse of the structure along **c**. The space group was left unchanged, the *c*-dimension shortened, and the relationships between atoms within the layers maintained. As in refinement of the 8.7 Å phase, the (002) reflection was excluded. The final fit is shown in Figure 5b, refinement parameters in Table 2, and atom positions in Table 4. Refinement of P and As occupancies resulted in difficulties similar to those encountered with the 8.7 Å phase, thus they were fixed at 1 and 0, respectively.

The refined positions of the O atoms shared by the uranyl and phosphate polyhedra suggest that the polyhedra are rotated with respect to those of the 8.7 Å phase. In the 8.7 Å phase, the polyhedra from one sheet are not aligned with those of the next. In the 8.3 Å phase, the extent of misalignment is reduced (Figs. 1a and 1c). The squares formed by the H_2O oxygen atoms rotated about the Cu atoms in the transformation (Figs. 1b and 1d).

In the 8.7 Å phase, Cu is coordinated axially by O atoms of the uranyl groups in the adjacent sheets, and by 4 equatorial H_2O molecules, forming a distorted octahedron in which the distortion is partly due to Jahn-Teller effects (i.e., long axial and shorter equatorial bonds). In the 8.3 Å phase, this octahedron is maintained but the degree of distortion is lessened due to the collapse in basal spacing. Cu-O_{axial} bond lengths changed from

TABLE 4. Atomic coordinates and isotropic displacement parameters for the 8.3 Å phase (129 °C)

Atom	x	y	z	U_{iso} (Å^2)	Occ.
Cu1	0.25	0.25	0.2999(7)	0.0135(34)	0.881(17)
O1	0.25	0.25	0.4485(15)	0.01*	1
O2	0.25	0.25	0.9400(15)	0.01*	1
O3	0.25	0.25	0.6588(15)	0.01*	1
O4	0.25	0.25	0.1519(15)	0.01*	1
O5	0.304(5)	0.9096(34)	0.0579(19)	0.022(5)	1
O6	0.266(12)	0.9319(30)	0.5515(17)	0.022(5)	1
O7 (water)	0.559(4)	0.172(4)	0.2989(29)	0.03†	0.69(4)
O8 (water)	0.3396(33)	0.455(4)	0.8059(19)	0.03†	0.841(34)
P1	0.25	0.75	0	0.0133(24)	1
P2	0.25	0.75	0.5	0.0133(24)	1
U1	0.25	0.25	0.04955(31)	0.0135(4)	1
U2	0.25	0.25	0.55328(28)	0.0135(4)	1

* U_{iso} for O1–O4 and O7 refined to negative, or near zero, values, so they were fixed at 0.01 Å^2.
† U_{iso} for O8 refined to unrealistically large values, so that value and the U_{iso} for O7 were fixed at 0.03 Å^2, the value reported for water O atoms by Locock and Burns (2003).

2.39(2) and 2.68(2) Å in the 8.7 Å phase to 2.48(3) and 2.47(3) Å in the 8.3 Å phase, which represents an average decrease, and results in more equal bond lengths. A concomitant increase was observed in the mean equatorial (Cu-H_2O) bond lengths, from 1.95(1) to 2.22(3) Å. The apparent lessening of the Jahn-Teller distortion is almost certainly due, at least in part, to the difficulty in locating O atoms. However, the refinement indicates a loss of Cu from the structure, and such loss could lead to relaxation of the water positions about the Cu site. There are two symmetrically independent H_2O molecules in the metatorbernite structure. One (O7) comprises the square of equatorial H_2O molecules around the Cu atom and the other (O8) comprises a square with no central cation. The refined Cu, O7, and O8 occupancies decrease in the transformation between the 8.7 and 8.3 Å phases. This is in contrast to the inference of Suzuki et al. (2005) that O7 was retained in their 8.07 Å phase while O8 was lost. Rietveld refinement might not provide a complete answer as to which H_2O molecules are lost or the extent to which Cu is mobile during metatorbernite dehydration, but the refined occupancies presented here suggest that further study is warranted.

The total H_2O occupancy for the 8.3 Å phase refined to 6.1 H_2O per formula unit (pfu), in agreement with the DTA/TGA results of Frost et al. (2005), who reported 6.5 H_2O pfu in a phase that formed at 138 °C. Our refined H_2O occupancy for this phase exceeds the DTA/TGA results reported by Suzuki et al. (2005) (4–5 H_2O pfu; 8.07 Å basal spacing; 100 °C); Suzuki et al. (1998) (4 H_2O pfu; 8.2 Å basal spacing; 55–85 °C); and Vochten et al. (1981) (4 H_2O pfu; 120 °C).

6.9 Å phase. Although the 6.9 Å phase first appeared at 138 °C and was still present at 315 °C, it occurred as a single phase (i.e., not mixed with either the 8.3 or 5.4 Å phase) only between 173 and 200 °C. The diffraction pattern collected at 173 °C was used for the determination and refinement of the structure. Initial work on the 6.9 Å phase focused on maintaining the autunite-type sheet topology. The peak positions could not be matched in the tetragonal crystal system, but several monoclinic space groups with $a \approx 6.6$, $b \approx 7.0$, $c \approx 14$ Å, and $\beta \approx$ either 98° or 107° matched the peak positions well. Models were constructed using CrystalMaker software in which several variations on the stacking of the autunite-type sheets were proposed. Le Bail fits were carried out to determine likely unit-cell, background,

and peak profile parameters. Bond length and angle restraints were set within given polyhedra, and Rietveld refinement used to adjust atom positions. Unit-cell, background, zero-shift, and peak profile parameters were then further refined. Refinements of these structures failed to converge and produced cation and anion topologies that were inconsistent with autunite-type sheets.

Although these refinements failed, the structure models generated by them, as well as attempts made for the 5.4 Å phase (see below), provided important clues about the nature of our proposed structure described below. The positions of the U atoms, which are arranged in a pattern that is corrugated in two dimensions in autunite-type sheets, consistently refined in a manner that suggested the U atoms within each sheet in the 6.9 Å phase might be nearly coplanar. Such an arrangement of U atoms is impossible in an autunite-type sheet. In addition, the U and P atoms, when viewed along [001] in the 8.7 and 8.3 Å phases (ignoring the corrugations in the **c**-direction), occur in linear arrays. Several attempts at refining several proposed structure models in several space groups for the 6.9 Å phase resulted in zigzag U-P patterns (when viewed along [001]). Furthermore, the O atoms shared by the U and P polyhedra failed to retain the square arrangement about the U atoms characteristic of autunite-type sheets.

Careful examination of the poorly refined structures generated in these first efforts suggested that a minor rearrangement of O atoms within the sheets could yield chains of uranyl pentagonal bipyramids. Such chains are common in the uranophane group of uranyl silicate minerals (Burns 2005). These structures involve chains of edge-sharing uranyl pentagonal bipyramids (Fig. 1e) joined into sheets by the sharing of edges and vertices with phosphate tetrahedra. An automatic peak search to match the powder pattern of the 6.9 Å phase was run using the program Jade (Materials Data, Inc.) and the ICDD powder diffraction database. Boltwoodite [$K(H_3O)(UO_2)(SiO_4)$; ICDD 083-1848], which is a uranophane-group mineral, appeared in the top 15 structural matches, supporting the hypothesis that the 6.9 Å structure contains uranophane-type sheets.

Several uranophane-group minerals were tried as starting structures for the 6.9 Å phase, as follows: In CrystalMaker files, P was substituted for Si, lattice parameters were adjusted to match the observed peak positions, and U and P polyhedra were adjusted to have physically reasonable bond lengths and angles. Predicted powder patterns were plotted in the program CrystalDiffract to check for broad agreement with the observed patterns before Rietveld refinements were attempted. Kasolite, boltwoodite, and α-uranophane, in which the stacking of uranophane-type sheets is the same, were more successful starting structures than β-uranophane, sklodowskite, cuprosklodowskite, and ulrichite. Of these, the structure modeled on that of α-uranophane in space group $P2_1$ with $\beta \approx 107°$ produced the best fit. In this structure and cell setting, the (100) plane is parallel to the sheets, rather than (001) as in room-temperature metatorbernite. The axes in the 6.9 Å phase were therefore transformed to follow the convention in α-uranophane.

Once the structure model, minus Cu and H_2O, had been partially refined, the Cu atoms and H_2O oxygen atoms were located using Fourier difference maps, and then their positions and occupancies were refined. The final fit is shown in Figure 5c, refinement parameters in Table 2, and atom positions in Table 5. Values of χ^2, R_{wp}, and $R(F^2)$ all suggest a good fit of the model to the data, and are comparable to the values for the low-temperature structures. Occupancies for the three H_2O oxygen atoms all refined to values slightly larger than 1 and were therefore fixed at 1. Refinement of P and As occupancies resulted in difficulties similar to those encountered with the 8.7 Å phase, thus they were fixed at 1 and 0, respectively. The model structure of the 6.9 Å phase is shown in Figures 1e–1f. As in the 8.7 and 8.3 Å phases, the unit cell for this structure contains two symmetrically independent U and P atoms. U1 and P1 occupy the layer at the base of the unit cell ($x \approx 0$), while U2 and P2 occupy the layer at the center of the cell ($x \approx 0.5$). The refined positions and orientations of the P tetrahedra in the two layers are different, as seen when the structure is viewed along [010] (Fig. 1f). The P atoms of the "even" layer (P2) are nearly coplanar, while those of the "odd" layer (P1) lie ~0.05 Å either side of the plane at $x \approx 0$. It is possible that this difference in orientations is an artifact resulting from the difficulty in locating lighter atoms in a U-rich structure and from the bond distance and angle restraints set at the beginning of the refinement.

The equatorial O atoms in the uranyl polyhedra of the refined structure for the 6.9 Å phase are distorted from ideal pentagons. Although some of the noted distortion is likely an artifact of the difficulty in determining accurate oxygen positions, the U polyhedra are not expected to be regular, because each U pentagonal bipyramid shares an edge with a P tetrahedron. An ideal uranium pentagon with $U\text{-}O_{equatorial}$ bond distances ~2.4 Å (cf. Burns 2005) would have edges ~2.8 Å long. This is a good match for edge lengths typical of Si tetrahedra, and the polyhedra in the uranophane-group silicates are therefore relatively regular. The edge of a typical P tetrahedron, however, is ~2.4–2.5 Å (Baur 1974), requiring distortion of the U polyhedra.

Our refinement (after relaxing bond angle and distance restraints) suggests a lengthening of the bonds between U and the O atoms of the shared edge, from ~2.4 Å in a typical uranyl bipyramid to ~2.6 Å in the "odd" layer and ~2.8 Å in the "even" layer. The edges shared with the P tetrahedra are 2.49 and 2.43 Å long, respectively.

TABLE 5. Atomic coordinates and isotropic displacement parameters for the 6.9 Å phase (173 °C)

Atom	x	y	z	U_{iso} (Å²)	Occ.
Cu1	0.2324(22)	0.475(4)	0.527(5)	0.008(5)	0.930(17)
O1	0.1461(21)	0.844(7)	0.227(8)	0.01*	1
O2	0.3627(20)	0.245(8)	0.774(9)	0.01*	1
O3	–0.1081(21)	0.730(8)	0.086(7)	0.01*	1
O4	0.6234(20)	0.206(8)	0.889(8)	0.01*	1
O5	0.0542(30)	0.469(4)	0.202(5)	0.01*	1
O6	0.5189(31)	0.539(4)	0.801(5)	0.01*	1
O7	0.0130(32)	0.125(4)	0.202(5)	0.01*	1
O8	0.5060(32)	0.884(4)	0.773(5)	0.01*	1
O9	–0.0110(24)	0.339(7)	0.491(4)	0.01*	1
O10	0.5654(22)	0.703(7)	0.519(4)	0.01*	1
O11	0.1596(21)	0.250(7)	0.472(6)	0.01*	1
O12	0.3844(22)	0.689(7)	0.497(6)	0.01*	1
O13 (water)	0.749(10)	–0.041(13)	0.042(13)	0.01*	1
O14 (water)	0.701(5)	–0.191(13)	0.724(9)	0.01*	1
O15 (water)	0.731(8)	0.499(11)	0.792(13)	0.01*	1
P1	0.0559(12)	0.2993(27)	0.3491(27)	0.027(7)	1
P2	0.4918(12)	0.7013(28)	0.6356(27)	0.027(7)	1
U1	0.0188(5)	0.7894(9)	0.1541(8)	0.01140(18)	1
U2	0.4942(4)	0.2192(9)	0.8375(8)	0.01140(18)	1

* U_{iso} for all O atoms refined to negative or near zero values, so they were fixed at 0.01 Å².

Although uranophane-type sheets have not been found in uranyl phosphate minerals, they have been described in synthetic inorganic uranyl phosphates (Locock and Burns 2002a, 2002b, 2004a; Locock 2007), mixed organic-inorganic uranyl phosphates (Francis et al. 1998; Danis et al. 2001; Locock and Burns 2004b), and uranyl phosphonates (Poojary et al. 1995; Grohol et al. 1999; Knope and Cahill 2008). These phases contain uranyl pentagonal bipyramids that are distorted as follows: The edges shared with phosphate tetrahedra are 2.3–2.5 Å long (as opposed to 2.8 Å in undistorted bipyramids), and the bonds between U and the O atoms of the edges shared with the tetrahedra are ~2.5–2.6 Å long (as opposed to 2.4 Å in undistorted bipyramids). Similar polyhedral distortion was also described by Forbes and Burns (2006) in the uranophane-type structure of $Ba(NpO_2)(PO_4)\cdot H_2O$. The 2.8 Å $U\text{-}O_{equatorial}$ bond refined in the current study is exceptionally long, and its apparent length may have been exaggerated by difficulties in determining O positions. However, the general form of distortion, i.e., the shortening of the U pentagonal bipyramid edges shared with P, and the lengthening of the $U\text{-}O_{equatorial}$ bonds for those O atoms shared with P, is consistent across the refinements presented here and the previously determined structures.

The reconstruction of the sheets from those in the 8.3 Å structure to those in the 6.9 Å phase may be explained by examining the morphologies of the two sheet types. Autunite-type sheets are corrugated in two dimensions (along **a**), with morphologies like egg cartons (Figs. 1a–1b). In the 8.7 and 8.3 Å phases, the sheets are arranged in the manner that would allow their closest possible packing (i.e., the way in which one would stack egg cartons). Upon removal of sufficient interlayer H_2O, it must be energetically favorable for the sheets to approach one another more closely than is allowed by the approach of the uranyl-group O atoms from one sheet to those of the next. Simply allowing the autunite-type sheets to be assembled more closely together would result in uranyl apical O-O distances of ~3.2 Å. This distance is slightly longer than the sheet-to-sheet O-O distances in phyllosilicates like talc and pyrophyllite (~3.1 Å), but it does not leave sufficient space for an interlayer cation. Uranophane-type sheets are uncorrugated, and hence, flatter. They can, therefore, be stacked more closely than autunite-type sheets.

In the 6.9 Å phase, the Cu-coordination environment is difficult to determine, because of the uncertainty in the positions of the O atoms, but a highly distorted octahedron can be drawn with O1 and O2 (of uranyl groups from adjacent sheets) as the axial O atoms and O11 and O12 (tetrahedral apices) and O13 and O14 (H_2O molecules) as the equatorial O atoms. Uncertainties in Cu occupancies likely exceed those estimated in the refinement, given the correlations between occupancies, temperature factors, and background, and the difference between the Cu occupancies in the 8.3 and 6.9 Å phases (refined as 0.88 and 0.93, respectively) is probably not significant.

The total H_2O occupancy in the 6.9 Å phase at 173 °C refined to 3 H_2O pfu, in excess of the 2 H_2O pfu reported by Suzuki et al. (2005) (6.58 Å basal spacing; 200 °C); Suzuki et al. (1998) (6.8 Å basal spacing; 65–270 °C); Vochten et al. (1981) (150 °C; 0 H_2O pfu at $T > 150$ °C); and Frost et al. (2005) (155 °C; 0 H_2O pfu at $T > 150$ °C). It is likely that the experimental design, combined with the large uncertainties in occupancy factors, contributed to these differences.

Refinement of the 6.9 Å structure model at 191 °C resulted in a structure nearly identical to that of the phase at 173 °C, with modest decrease in the *a*-dimension (by 0.0103 Å), expansion in *b* and *c* (by 0.0021 and 0.0029 Å, respectively), increase in β of 0.031°, and no detected loss of interlayer H_2O.

5.4 Å phase. Several structures based on the 6.9 Å phase (containing uranophane-type sheets) were proposed for the 5.4 Å phase. Le Bail fits were conducted for unit cells in several monoclinic and triclinic space groups, and suggest unit-cell dimensions ~6.7, 7, and 11 Å and $\beta \approx 100°$. None of the proposed structures resulted in Rietveld refinement convergence on a physically reasonable structure. Nevertheless, preliminary results suggest the presence of uranyl pentagonal bipyramids. Future studies will focus on the development and refinement of structural models to describe the 5.4 Å phase.

ACKNOWLEDGMENTS

This research was supported by U.S. Department of Energy, Basic Energy Sciences Grant no. DEFG02-89ER14074 to D.R.V. and D.C.E., NSF Grant no. EAR07-45374 to P.J.H. and J.E.P., and the Center for Environmental Kinetics Analysis (CEKA), an NSF- and DOE-sponsored Environmental Molecular Science Insititute (NSF Grant no. CHE04-31328 to P.J.H.). Use of the National Synchrotron Light Source, Brookhaven National Laboratory, was supported by the U.S. Department of Energy, Office of Science, Office of Basic Energy Sciences, under Contract no. DEAC02-98CH10886. We thank Peter Burns for commenting on an earlier draft of the manuscript. We thank our AE, Aaron Celestian, and three anonymous reviewers for their helpful suggestions.

REFERENCES CITED

Arai, Y., Marcus, M.K., Tamura, N., Davis, J.A., and Zachara, J.M. (2007) Spectroscopic evidence for uranium bearing precipitates in vadose zone sediments at the Hanford 300-area site. Environmental Science and Technology, 41, 4633–4639.

Baur, W.H. (1974) The geometry of polyhedral distortions. Predictive relationships for the phosphate group. Acta Crystallographica Section B-Structural Science, B30, 1195–1215.

Beintema, J. (1938) On the composition and the crystallography of autunite and the meta-autunites. Recueil Des Travaux Chimiques Des Pays-Bas, 57, 155–175.

Buck, E.C., Dietz, N.L., and Bates, J.K. (1995) Uranium-contaminated soils—ultramicrotomy and electron-beam analysis. Microscopy Research and Technique, 31, 174–181.

Buck, E.C., Brown, N.R., and Dietz, N.L. (1996) Contaminant uranium phases and leaching at the Fernald site in Ohio. Environmental Science and Technology, 30, 81–88.

Burns, P.C. (2005) U^{6+} minerals and inorganic compounds: Insights into an expanded structural hierarchy of crystal structures. Canadian Mineralogist, 43, 1839–1894.

Butt, C.R.M. and Graham, J. (1981) Sodian potassian hydroxonian meta-autunite: first natural occurrence of an intermediate member of a predicted solid solution series. American Mineralogist, 66, 1068–1072.

Catalano, J.G., McKinley, J.P., Zachara, J.M., Heald, S.M., Smith, S.C., and Brown, G.E. (2006) Changes in uranium speciation through a depth sequence of contaminated Hanford sediments. Environmental Science and Technology, 40, 2517–2524.

Danis, J.A., Runde, W.H., Scott, B., Fettinger, J., and Eichhorn, B. (2001) Hydrothermal synthesis of the first organically templated open-framework uranium phosphate. Chemical Communications, 2378–2379.

Finger, L.W., Cox, D.E., and Jephcoat, A.P. (1994) A correction for powder diffraction peak asymmetry due to axial divergence. Journal of Applied Crystallography, 27, 892–900.

Forbes, T.Z. and Burns, P.C. (2006) $Ba(NpO_2)(PO_4)(H_2O)$, its relationship to the uranophane group, and implications for Np incorporation in uranyl minerals. American Mineralogist, 91, 1089–1093.

Francis, R.J., Drewitt, M.J., Halasyamani, P.S., Ranganathachar, C., O'Hare, D., Clegg, W., and Teat, S.J. (1998) Organically templated layered uranium(VI) phosphates: hydrothermal syntheses and structures of $[NHEt_3][(UO_2)_2(PO_4)(HPO_4)]$ and $[NPr_4][(UO_2)_3(PO_4)(HPO_4)_2]$. Chemical Communications, 279–280.

Frost, R.L., Kristof, J., Weier, M.L., Martens, W.N., and Horvath, E. (2005) Thermal decomposition of metatorbernite—A controlled rate thermal analysis study.

Journal of Thermal Analysis and Calorimetry, 79, 721–725.
Graham, J., Butt, C.R.M., and Vigers, R.B.W. (1984) Sub-surface charging, a source of error in microprobe analysis. X-ray Spectrometry, 13, 126–133.
Grohol, D., Gingl, F., and Clearfield, A. (1999) Syntheses and crystal structures of a linear-chain uranyl phenylphosphinate $UO_2(O_2PHC_6H_5)_2$ and layered uranyl methylphosphonate $UO_2(O_3PCH_3)$. Inorganic Chemistry, 38, 751–756.
Hammersley, A.P., Svensson, S.O., Hanfland, M., Fitch, A.N., and Hausermann, D. (1996) Two-dimensional detector software: From real detector to idealised image or two-theta scan. High Pressure Research, 14, 235–248.
Jerden, J.L. and Sinha, A.K. (2003) Phosphate based immobilization of uranium in an oxidizing bedrock aquifer. Applied Geochemistry, 18, 823–843.
Jerden, J.L., Sinha, A.K., and Zelazny, L. (2003) Natural immobilization of uranium by phosphate mineralization in an oxidizing saprolite-soil profile: chemical weathering of the Coles Hill uranium deposit, Virginia. Chemical Geology, 199, 129–157.
Knope, K.E. and Cahill, C.L. (2008) Structural variation within homometallic uranium(VI) carboxyphosphonates: In situ ligand synthesis, directed assembly, metal-ligand coordination and hydrogen bonding. Inorganic Chemistry, 47, 7660–7672.
Larson, A.C. and Von Dreele, R.B. (2004) General Structure Analysis System (GSAS). Los Alamos Natonal Laboratory, Report LAUR 86-748.
Le Bail, A., Duroy, H., and Fourquet, J.L. (1988) Ab-initio structure determination of $LiSbWO_6$ by X-ray powder diffraction. Materials Research Bulletin, 23, 447–452.
Locock, A.J. (2007) Crystal chemistry of actinide phosphates and arsenates. In S.V. Krivovichev and P.C. Burns, Eds., Structural Chemistry of Inorganic Actinide Compounds, p. 217–278. Elsevier, Amsterdam.
Locock, A.J. and Burns, P.C. (2002a) Crystal structures of three framework alkali metal uranyl phosphate hydrates. Journal of Solid State Chemistry, 167, 226–236.
——— (2002b) The crystal structure of triuranyl diphosphate tetrahydrate. Journal of Solid State Chemistry, 163, 275–280.
——— (2003) Crystal structures and synthesis of the copper-dominant members of the autunite and meta-autunite groups: Torbernite, zeunerite, metatorbernite and metazeunerite. Canadian Mineralogist, 41, 489–502.
——— (2004a) Revised Tl(I)-O bond valence parameters and the structures of thallous dichromate and thallous uranyl phosphate hydrate. Zeitschrift für Kristallographie, 219, 259–266.
——— (2004b) Structures and syntheses of layered and framework amine-bearing uranyl phosphate and uranyl arsenates. Journal of Solid State Chemistry, 177, 2675–2684.
Locock, A.J., Burns, P.C., and Flynn, T.M. (2005) Structures of strontium- and barium-dominant compounds that contain the autunite-type sheet. Canadian Mineralogist, 43, 721–733.
Murakami, T., Ohnuki, T., Isobe, H., and Sato, T. (1997) Mobility of uranium during weathering. American Mineralogist, 82, 888–899.
Murakami, T., Sato, T., Ohnuki, T., and Isobe, H. (2005) Field evidence for uranium nanocrystallization and its implications for uranium transport. Chemical Geology, 221, 117–126.
Poojary, D.M., Grohol, D., and Clearfield, A. (1995) Crystal-structure of uranyl chloromethylphosphonate from X-ray powder diffraction data. Journal of Physics and Chemistry of Solids, 56, 1383–1388.
Ross, M., Evans, H.T., and Appleman, D.E. (1964) Studies of torbernite minerals 2. Crystal structure of meta-torbernite. American Mineralogist, 49, 1603–1621.
Sato, T., Murakami, T., Yanase, N., Isobe, H., Payne, T.E., and Airey, P.L. (1997) Iron nodules scavenging uranium from groundwater. Environmental Science and Technology, 31, 2854–2858.
Singer, D.M., Zachara, J.M., and Brown, G.E. (2009) Uranium speciation as a function of depth in contaminated Hanford Sediments: A micro-XRF, micro-XRD, and micro- and bulk-XAFS study. Environmental Science and Technology, 43, 630–636.
Sowder, A.G., Clark, S.B., and Fjeld, R.A. (2000) Dehydration of synthetic autunite hydrates. Radiochimica Acta, 88, 533–538.
Stephens, P.W. (1999) Phenomenological model of anisotropic peak broadening in powder diffraction. Journal of Applied Crystallography, 32, 281–289.
Stergiou, A.C., Rentzeperis, P.J., and Sklavounos, S. (1993) Refinement of the crystal-structure of metatorbernite. Zeitschrift für Kristallographie, 205, 1–7.
Stormer, J.C., Pierson, M.L., and Tacker, R.C. (1993) Variation of F and Cl X-ray intensity due to anisotropic diffusion in apatite during electron microprobe analysis. American Mineralogist, 78, 641–648.
Stubbs, J.E. (2009) Mineralogical and geochemical studies of uranium-contaminated soils and uranium phosphate minerals. Ph.D. thesis, Johns Hopkins University, Baltimore, Maryland.
Stubbs, J.E., Elbert, D.C., Veblen, D.R., and Zhu, C. (2006) Electron microbeam investigation of uranium-contaminated soils from Oak Ridge, Tennessee, U.S.A. Environmental Science and Technology, 40, 2108–2113.
Stubbs, J.E., Elbert, D.C., Veblen, L.A., and Veblen, D.R. (2007) Rapid cation depletion during electron microprobe analysis of uranium phosphates. Eos Transactions AGU, 88, Fall Meeting Supplemental, Abstract V51A-0324.
Stubbs, J.E., Veblen, L.A., Elbert, D.C., Zachara, J.M., Davis, J.A., and Veblen, D.R. (2009) Newly recognized hosts for uranium in the Hanford Site vadose zone. Geochimica et Cosmochimica Acta, 73, 1563–1576.
Suzuki, Y., Murakami, T., Kogure, T., Isobe, H., and Sato, T. (1998) Crystal chemistry and microstructures of uranyl phosphates. Materials Research Society Symposia Proceedings, 506, 839–846.
Suzuki, Y., Sato, T., Isobe, H., Kogure, T., and Murakami, T. (2005) Dehydration processes in the meta-autunite group minerals meta-autunite, metasaleeite, and metatorbernite. American Mineralogist, 90, 1308–1314.
Takano, Y. (1961) X-ray study of autunite. American Mineralogist, 46, 812–822.
Thompson, P., Cox, D.E., and Hastings, J.B. (1987) Rietveld refinemeent of Debye-Sherrer synchrotron X-ray data from Al_2O_3. Journal of Applied Crystallography, 20, 79–83.
Toby, B.H. (2001) EXPGUI, a graphical user interface for GSAS. Journal of Applied Crystallography, 34, 210–213.
Vochten, R., Piret, P., and Goeminne, A. (1981) Synthesis, crystallographic data, solubility and electrokinetic properties of copper-uranylphosphate, nickel-uranylphosphate and cobalt-uranylphosphate. Bulletin de Mineralogie, 104, 457–467.
Zachara, J.M., Serne, J., Freshley, M., Mann, F., Anderson, F., Wood, M., Jones, T., and Myers, D. (2007) Geochemical processes controlling migration of tank wastes in Hanford's vadose zone. Vadose Zone Journal, 6, 985–1003.

Manuscript received October 31, 2009
Manuscript accepted April 19, 2010
Manuscript handled by Aaron Celestian